Proton capture resonant state of ^{15}O at 7556 keV

Sathi Sharma,[1] Arkabrata Gupta,[2] M. Roy Chowdhury,[3] A. Mandal,[3] A. Bisoi,[2] V. Nanal,[3] L. C. Tribedi,[3] and M. Saha Sarkar[1,*]

[1]*Saha Institute of Nuclear Physics, HBNI, 1/AF Bidhannagar, Kolkata - 700 064, India*

[2]*Indian Institute of Engineering Science and Technology, Shibpur, Howrah - 711 103, India*

[3]*Department of Nuclear and Atomic Physics, Tata Institute of Fundamental Research, Colaba, Mumbai - 400 005, India*

(Received 19 June 2020; accepted 20 July 2020; published 6 August 2020)

The slowest reaction in the CNO cycle ^{14}N$(p,\gamma)^{15}$O has been studied by populating the $E_p^{\rm lab} = 278$ keV ($E^r_{\rm c.m.} = 259$ keV) proton capture resonant state of ^{15}O at 7556 keV. The strength of the resonance ($\omega\gamma$) has been determined from the experimental data. The level lifetime of the subthreshold resonant state at $E_x = 6792$ keV, as well as the lifetimes of the 5181 keV and 6172 keV states, have been measured using the Doppler shift attenuation method (DSAM). The structural properties of the nucleus ^{15}O, such as the level energies, transition strengths, level lifetimes, and spectroscopic factors, have been calculated theoretically by using the large basis shell model, which agrees reasonably well with the present as well as the previous experimental data.

DOI: 10.1103/PhysRevC.102.024308

I. INTRODUCTION

The study of nuclear reactions relevant to the nucleosynthesis process is very important to trace the origin and evolution of the different elements and to provide a stringent test to theoretical models [1]. In the first evolutionary stage of stars, the energy production mainly occurs via hydrogen burning inside the core through the PP (proton-proton) chain. The low metallicity population II stars with the mass $M > 1.5M_{\rm solar}$, initiate hydrogen burning via the CNO (carbon-nitrogen-oxygen) cycle along with the PP chain. The CNO cycle reactions have the same end-product, i.e., ^{4}He as that for the PP chain. The C, N, O, or F nuclei act only as catalysts, as their total abundances are not altered while only the hydrogen is consumed. Due to the highest Coulomb barrier ($\sim$2460 keV) of the ^{14}N$(p,\gamma)^{15}$O reaction, it is the slowest reaction or the bottleneck of the CNO cycle I. So, this reaction plays a vital role in the stellar energy production and the reaction rate determination. The CNO cycles II, III, and IV do not contribute much to the energy production due to the higher Coulomb barrier. The globular clusters provide a strict constraint for the stellar models [1] because of their distinct features in the Hertzsprung Russell (H-R) diagram. The age of the globular cluster can be determined from the main sequence (MS) turn off point, which is related to the ^{14}N$(p,\gamma)^{15}$O reaction rate. The lower limit of the age of the universe is also estimated from the globular cluster age determination [2]. There are many other implications of the ^{14}N$(p,\gamma)^{15}$O reaction which are discussed elaborately in Refs. [1–4].

Schröder *et al.* [5] studied the ^{14}N$(p,\gamma)^{15}$O direct capture reaction in the energy range of $E_p = 200$–3600 keV. After analyzing the cross-section data, they suggested a significant contribution of the $E_{\rm c.m.} = -504$ keV subthreshold resonance state at 6792 keV of ^{15}O in the total astrophysical S factor at zero energy, i.e., $S(0)$ value. They had kept the γ-ray width (Γ_γ) as a free parameter in the theoretical fit and obtained the width as 6.3 eV. The R-matrix analysis was performed by Angulo *et al.* [6] with all the previously measured data. They got a completely different value of the radiative width of the 6792 keV subthreshold resonant state. The value of Γ_γ was 3.6 times less than the value mentioned by Schröder *et al.* [5]. The discrepancy between the value of radiative width (Γ_γ) motivated experimentalists and theoreticians to do new experiments and R-matrix fits.

If an excited state decays with nearly 100% probability via the emission of γ rays, then it is possible to obtain the total radiative width Γ ($\simeq\Gamma_\gamma$) by measuring the lifetime (τ) of the state. They are inversely related via the relation, $\Gamma = \hbar/\tau$. Bertone *et al.* [7] measured the lifetimes of the 5181 keV, 6172 keV, and 6792 keV states of the nucleus ^{15}O using the Doppler shift attenuation method (DSAM). The measured lifetime of the 6792 keV state was $1.60^{+0.75}_{-0.72}$ fs, which included the statistical uncertainties. However, if they had used the implanted target density corresponding to the compound TaN instead of the Ta, the change in stopping power would have resulted in a higher value of lifetime, 3.2 ± 1.5 fs. In Ref. [8], Schürmann *et al.* had used the same centroid shift method with data at 11 different angles with better statistics. But they could only set an upper limit in the lifetime value ($\tau <$ 0.77 fs). The latest value of the experimental lifetime of the 6792 keV state was obtained by Galinski *et al.* [9] using the inverse kinematics. They have used the ^{3}He$(^{16}$O$,\alpha)^{15}$O reaction to populate the excited state of ^{15}O at a beam energy of 50 MeV with maximum recoil velocity $\beta = 0.05$. As the maximum recoil velocity is 5% of the speed (c) of light in vacuum, a Monte Carlo code was written using the relativistic kinematics to obtain the lifetime value. Using the maximum

*maitrayee.sahasarkar@saha.ac.in

 ©2020 American Physical Society

likelihood method, they got an upper limit of $\tau < 1.84$ fs, which corresponds to a lower bound on the width, i.e., $\Gamma > 0.44$ eV. Therefore in Ref. [9], they gave only the upper limit of the lifetime of the 6792 keV state using the data only at one angle, which was at 0°. Thus, the lifetimes determined using the centroid shift method described in Refs. [8,9] gave different results. So, uncertainty remains in the central value of the lifetime of the subthreshold resonant state.

In our present work, we have therefore measured the lifetime of the subthreshold state by populating it via ^{14}N$(p,\gamma)^{15}$O resonance reaction at laboratory energy 278 keV. We have used the DSAM analysis (with the nonrelativistic kinematic equations), as discussed in Refs. [7,8]. The lifetimes of the 5181 keV, 6172 keV states of the nucleus ^{15}O have also been measured in this experiment. The resonance strength ($\omega\gamma$) of the 278 keV narrow resonance is determined using the experimental data.

The rate of the ^{14}N$(p,\gamma)^{15}$O reaction is a sensitive function of the structural properties of the ^{15}O nucleus. These structural properties should be obtained from experiments and validated by theory for more accurate inputs to the nuclear astrophysics models. Many experiments were performed to measure the astrophysically relevant properties of the ^{15}O nucleus; however, very few theoretical calculations were done so far. Thus we have also done large basis shell model calculations to study the low lying energy levels, level lifetimes, proton spectroscopic factors of ^{15}O nucleus up to the resonance state at 7556 keV. The calculations have been performed using NUSHELLX code [10]. The theoretical results for the excitation spectra, transition probabilities, level lifetimes and spectroscopic factors are compared with the present and other available experimental data [5].

II. EXPERIMENTAL DETAILS

A. The implanted target

One of the most effective technique to produce targets which are isotopically pure and can withstand high beam load over a long time is implantation technique [11,12]. $^{14}N^{3+}$ ions of energy 75 keV from the ECR (electron cyclotron resonance) ion source of the low energy ion accelerator [13–16] at Tata Institute of Fundamental Research (TIFR), Mumbai, were implanted into 0.30(5) mm thick Ta backing. Tantalum (Ta) was chosen as the backing material due to its low sputtering rate, high saturation value than other materials like Au, Cu, etc. The sputtering yield was simulated using TRIM simulation software [17]. The implantation has been done with a dose of 7.8×10^{17} atoms/cm^2. The beam was uniformly rastered over the Ta surface to have a uniform implantation circular zone with 2.5 cm diameter. Several techniques like x-ray photoelectron spectroscopy (XPS), scanning electron microscopy (SEM), secondary ion mass spectrometry (SIMS) have been used for surface characterization of the implanted target before and after implantation. The Ta backing was cleaned using ethanol and argon flashing before implantation to remove impurities in the backing. The SIMS analysis after 6 h of sputtering with 5 keV Cs ion, indicated that C, F, and Na contamination sharply decreased with increasing depth. However, oxygen impurity existed deep inside the backing. All the techniques discussed so far are reported in Refs. [18–21].

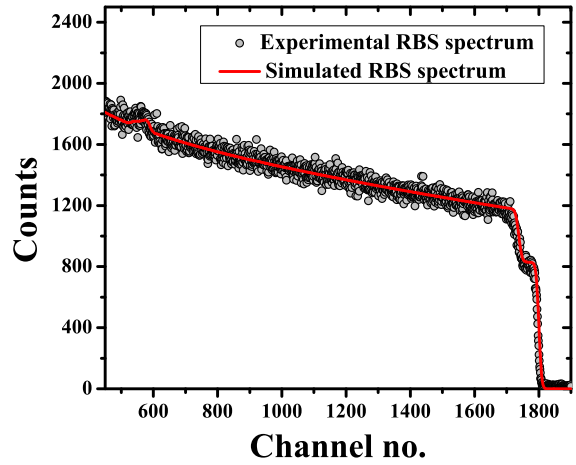

FIG. 1. A typical RBS spectrum of the implanted target. The SIMNRA fit [22] is shown in the solid red line.

The bulk characterization of the implanted target is done by Rutherford backscattering spectrometry (RBS) to get a quantitative estimation of the stoichiometry of the implanted target [20,21]. $^4He^{2+}$ ion beam with 3.65–3.70 MeV energy and 12.2 nA current from 1.7 MV Pelletron accelerator at Inter-University Accelerator Centre, New Delhi, was used to do the measurement. The scattered He ions were detected by a Si surface barrier detector placed at 165° with respect to the beam direction. The RBS spectra were acquired for both the ^{14}N implanted Ta and the bare Ta. The experimental spectra for the scattered ions from the implanted target bombarded with He ions at 3.682 MeV was fitted with the SIMNRA package [22] with stopping power from SRIM [17] as inputs. The best fit with reduced χ^2 value 1.0, was obtained with N:Ta concentration ratio as 3 : 2. The concentration ratio was determined with an uncertainty of less than 1%. The fitted plot is shown in Fig. 1. The Ta/N ratio for the implanted target is 0.667(33), which is similar to the target used by Daigle *et al.* [4] in a previous work.

B. Experimental setup and procedure

The ^{14}N$(p,\gamma)^{15}$O resonance experiment was performed at TIFR, Mumbai using ECRIA (ECR based ion accelerator) as mentioned in Sec. II A. The typical beam current on target during the experiment was 3–4 μA. The energy spread of the beam was 2–3 keV. The target was mounted at the end flange of the 0° beam line. As the beam current was not so high, there was no additional arrangement for cooling the target. The total charge collected during each run was measured using a current integrator.

Two detectors were used in the experiment. One of them was an electrically cooled CANBERRA (Mirion) Broad Energy Ge (BEGe) Falcon 5000 detector. The other one was a p-type LN_2 cooled high purity germanium (HPGe) detector from Baltic Scientific Instrument. The BEGe detector was cylindrical with a 3 cm radius and 3 cm in length with 18% relative efficiency. The LN_2 cooled HPGe detector was also

cylindrical with a 2.7 cm radius and 6.3 cm in length with 30% relative efficiency.

Both the detectors were placed at an angle of 90° to calibrate the in-beam spectra of the detectors. Standard radioactive source ^{152}Eu was used to calibrate the energy and efficiency of the detectors up to energy 1.5 MeV. For higher energy up to 7 MeV, calibrations were performed by using the in-beam γ rays emitted by the resonance state of ^{15}O [23].

While scanning the implanted target, the BEGe detector was placed at 1.7 cm from the target center at 0° to maximize the efficiency of the detector. The proton beam energy varied from 278 keV to 312 keV in steps of 3 keV each. The total charge accumulated in each run was estimated using a charge integrator.

However, for acquiring DSAM data for lifetime measurement, the proton energy was kept fixed at 293 keV. The BEGe detector was kept at 90° as well as at 0°, 25°, 50°, and 70° with respect to the beam direction. The other HPGe detector was placed at 90° as well as 120° and 137° to acquire lifetime measurement data. Both the detectors were placed at 5 cm from the target center. As the end flange was 1.3 cm thick, so the distance between the target and the detector was 6.3 cm. Both the detector responses were measured experimentally and compared with a GEANT4 simulation [24]. The beam spot had a shift from the central position in the end-flange (the position of the ^{152}Eu source during off-beam measurements). We have used the simulation to match the ^{152}Eu and in-beam resonance data for efficiency calibration of the detector over the whole energy range. The simulated data have been first matched with the experimental data, including the exact experimental conditions (the target position, the target holder geometry, etc.). Later the absolute efficiency of the detector is simulated for point sources. Thus, the effects of the target holder asymmetries, as well as source position mismatch, were eliminated. The relative and absolute efficiencies of the detectors were measured and compared with simulation. The GEANT4 simulation matched the experimental results within 1σ level of uncertainty. The characterization of the BEGe detector until 7 MeV has been described in details in Ref. [23]. The response of the HPGe detector was also obtained similarly. A comparison of the experimental and simulated energy spectra for the HPGe detector at an angle 90° is shown in Fig. 2.

The experimental data of the BEGe detector were acquired using the GENIE-2000 [25] data acquisition system (DAQ). It has a comprehensive set of capabilities for pulse processing, acquiring data, and analyzing spectra from multichannel analyzers (MCAs). MCA control, spectral display and manipulation, spectrum analysis, and reporting [25] are the basic functionalities of the DAQ system. The inherent gain of the setup was set to a minimum to acquire the γ-ray data till $\simeq 8$ MeV. The data were taken in 8k channels and singles mode. The analysis was done using GENIE-2000 [25] and an analysis software INGASORT [26]. For the HPGe detector, we had used a CAEN DT5780M (16 channel, 100 MS/s, 14 bit) digitizer [27] for pulse processing and data acquisition. The spectra were acquired in 16k channels and singles mode with minimum gain to have the data till 8 MeV to reduce the error in centroid determination.

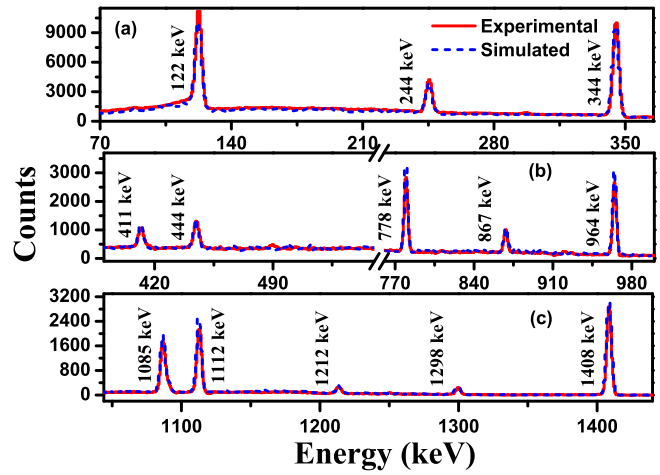

FIG. 2. Comparison of the experimental and simulated energy spectra of ^{152}Eu for HPGe detector at 90°. (a) Low (70–365 keV), (b) medium (390–1000 keV), and (c) high (1044–1440 keV) energy regions of the spectra are shown. The red solid line and blue dashed line connect the experimental and simulated data points, respectively.

III. RESULTS AND ANALYSIS

To calibrate the in-beam spectrum for both the detectors, we have used the data at 90° angle. The high energy part of the spectrum of the HPGe detector at 90° is shown in Fig. 3. The strong γ rays coming from room background (like 511 keV, 1460 keV, and 2615 keV) and γ rays emitted from the excited state (7556 keV) of ^{15}O nucleus have been used for calibration. The gain stability of the detectors and electronics were assured by continuous monitoring of the background γ lines. Two crucial experimental information have been obtained from the present data. They are

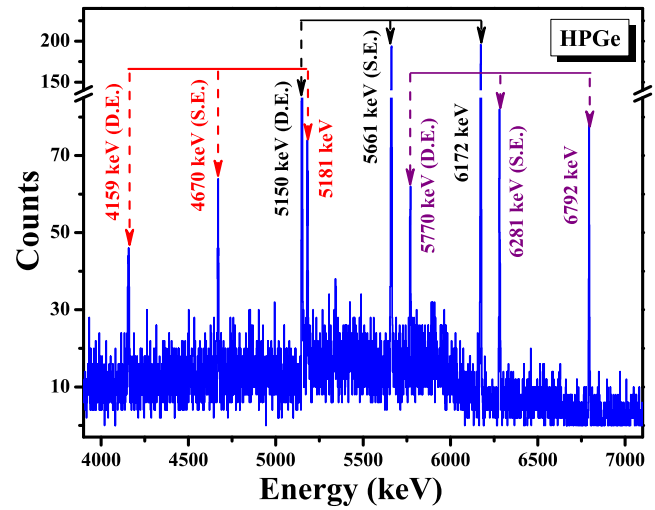

FIG. 3. Typical high-energy part of γ-ray energy spectrum from ^{14}N$(p,\gamma)^{15}$O resonance reaction at $E_p^{\rm lab} = 278$ keV of HPGe detector at an angle of 90°. S.E. and D.E. denote single escape and double escape peaks, respectively.

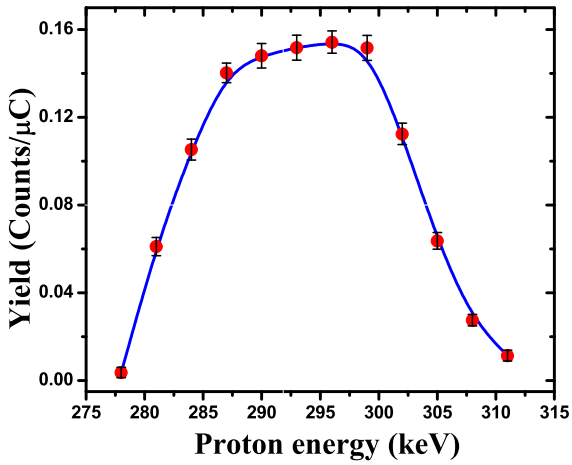

FIG. 4. γ-ray yield plot of the $E_p^{\rm lab} = 278$ keV resonance of $^{14}{\rm N}(p,\gamma)^{15}$ reaction. The solid blue line is a guide to the eye.

(i) the strength of the 259 keV resonance (7556 keV excited state) in ^{15}O populated by proton capture resonant reaction and
(ii) the lifetimes of the excited states of ^{15}O populated in the present resonance reaction by analyzing the centroid shifts of the associated γ rays due to Doppler shift.

A. Resonance strength

1. Yield curve analysis

As already discussed in the last section, while scanning the implanted target, proton energy was varied from 278 keV to 312 keV in steps of 3 keV. The BEGe detector was placed at 0° at a distance of 1.7 cm from the target center. The strongest primary γ ray of ^{15}O compound nucleus in $^{14}{\rm N}(p,\gamma)^{15}{\rm O}$ resonance reaction is 1384 keV. The yield of the reaction at a particular incident energy is given by

$$Y = \frac{N_{\rm reaction}}{N_{\rm beam}} = \frac{N_{\rm peak}}{BN_{\rm beam}W\eta_{\rm peak}}, \quad (1)$$

where $N_{\rm reaction}$ is the total number of reactions that occurred and $N_{\rm beam}$ is the total number of incident projectiles. B, $N_{\rm peak}$, W, and $\eta_{\rm peak}$ are the branching ratio (probability of emission of that particular γ ray per reaction), the total number of photons emitted by the state excited by the reaction (given by the area under the corresponding photopeak), the angular correlation, and the detector efficiency, respectively, for a specific nuclear transition. The yield has been determined by utilizing the area under the 1384 keV γ-ray photopeak in the spectrum at each beam energy, incorporating other necessary factors. The yields have been plotted as a function of incident proton beam energies (Fig. 4) to generate the yield curve. In the present yield plot, we got a plateau region from 288 keV to 300 keV. To compare the experimental yield profile with TRIM simulation [17], we have expressed the incident proton beam energy in terms of the linear thickness of the target, using SRIM stopping power [17]. The experimental profile matches with simulation considering the density of the target similar to Ta only. The analysis of the target scanning results has been discussed in detail in Ref. [21]. From the yield plot, the measured energy thickness (ΔE) of the implanted target was $\simeq 21 \pm 1$ keV.

TABLE I. Comparison of experimental resonance strength [$\omega\gamma$ (meV)] determined in the present work with earlier literature values. The uncertainties are quoted within brackets. The weighted average value is also shown.

	$\omega\gamma$ (meV)	
Reference	Measured	Average
Present work	12.8 (9)	
Ref. [4]	12.6 (3)	
Ref. [29]	12.8 (6)	
Ref. [30]	12.9 (9)	12.7 (2)
Ref. [31]	12.4 (9)	
Ref. [32]	13.7 (10)	

For a thick target, whose energy width is more than the energy width of the resonance, the resonance strength can be determined using the height of the plateau region in the yield curve. The resonance strength ($\omega\gamma$) and maximum yield for a thick target is related through the equation

$$\omega\gamma = \frac{2\epsilon_r}{\lambda_r^2} Y_{{\rm max},\Delta E\to\infty}, \quad (2)$$

where λ_r^2 is the corresponding de Broglie wavelength and ϵ_r is the effective stopping power at the resonance energy. For determining the resonance strength, effective stopping power at the resonance energy (ϵ_r) for Ta has been used in the present work.

As the energy thickness (ΔE) of our target is nearly 21 keV and the width Γ of the resonance is 0.99(10) keV [28], the ratio $\Delta E/\Gamma$ is $\approxeq$21. It has been shown in [1] that if the target thickness is $\simeq$20 times larger than the total resonance width ($\Delta E/\Gamma \simeq 20$), the maximum yield at the plateau is $\simeq$95% of the yield for an infinitely thick target and the full width at half-maximum (FWHM) of the yield curve is equal to the target thickness within 0.5%. The uncertainties in the resonance strength are both statistical as well as systematic. The sources of systematic errors are the amount of total the charge accumulated, target stoichiometry, the effective energy, and branching of the corresponding γ ray, etc. Including the uncertainties, the present value of the resonance strength is, $\omega\gamma = 12.78 \pm 0.29({\rm stat.}) \pm 0.92({\rm syst.})$ meV. The present experimental value has been compared with the previous values from literature in Table I. The weighted average value of the resonance strength ($\omega\gamma_{\rm average}$) is 12.7 (2) meV.

B. Lifetime measurement

When γ rays of particular energy are emitted from a recoiling nucleus, while it slows down through the target medium, their energies are shifted. The shifted energy depends on the initial recoil velocity (v_0), angle between the detector detecting the γ ray and the recoiling nucleus (θ), velocity attenuation factor [$F(\tau)$] and the correction factor (P) for the

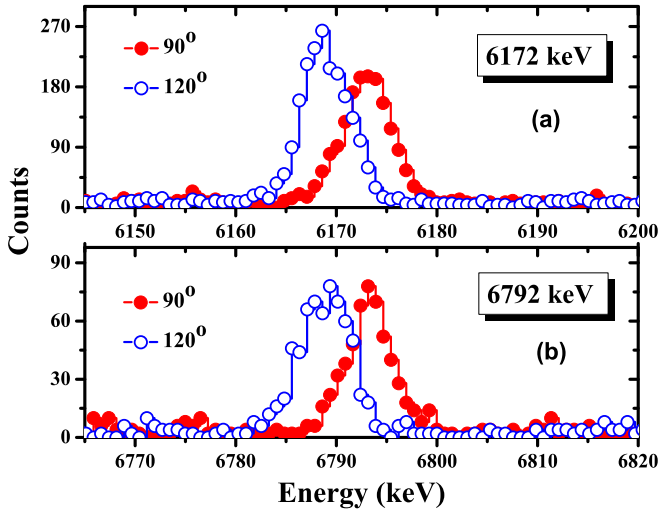

FIG. 5. Full energy peaks for (a) 6172 keV and (b) 6792 keV γ rays at two different angles of the HPGe detector. The red filled circles joined by red line and blue open circles joined by blue line correspond to the spectra at 90° and 120°, respectively.

finite size of the detector. The attenuation factor, $[F(\tau)]$, is a function of the lifetime of the nuclear level emitting the γ ray and the recoiling medium. The relation between the energy of the γ ray detected by the detector at an angle, θ, designated as (E_γ^θ) and actual energy of the γ ray (E_γ^o) is given by

$$E_\gamma^\theta = E_\gamma^o[1 + \beta_0 F(\tau) P \cos\theta], \tag{3}$$

where $\beta_0 = v_0/c$. The spectra acquired by the HPGe detector at 90° and 120° for 6172 keV and 6792 keV γ rays are shown in Fig. 5.

The reported energy width of the 7556 keV state (259 keV resonance state) is 0.99(10) keV [28]. The associated lifetime of the state is thus 0.66×10^{-18} s. This lifetime is too small compared to the stopping time of the recoiling nucleus in the medium, and thus the recoil velocity is not attenuated, i.e., $F(\tau) = 1$. For this reason, the lifetime of the resonance state could not be determined by the DSAM technique. However, the shifts of the primary γ rays emitted from this level have been utilized to determine the factor of $\beta_0 P$. The shifts of 1384 keV γ ray at different angles are plotted with $\cos\theta$, as shown in Fig. 6. The factor $\beta_0 P = 0.001738 \pm 0.000343$ has been obtained from a linear fit to the data points considering $F(\tau) = 1$. Next, the DSAM method is used to determine the lifetimes of the lower excited states of ^{15}O, from where the secondary γ rays originate. The centroids of three secondary γ rays 5181 keV, 6172 keV, and 6792 keV are determined at seven different angles. The shifted centroid values are plotted against $\cos\theta$. The angle (θ) values have been corrected to account for the shift of the beam spot from the center of the target flange. The plot for the 6792 keV γ ray is shown in Fig. 7. The data points have been fitted using Eq. (3). The $F(\tau)$ value for individual γ-ray energy (see Table II) has been determined after including the factor $\beta_0 P$ which was obtained from the linear fit shown in Fig. 6.

In general, the direction of motion of the recoil given by $\beta(t)$ at a particular time t will differ from that of $\beta(0)$ (at

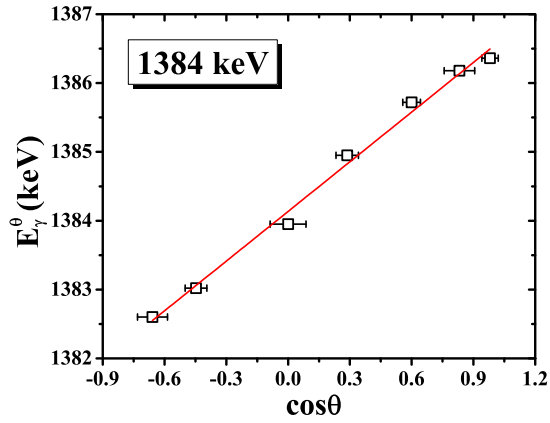

FIG. 6. Doppler shifted γ-ray energy (E_γ^θ) of 1384 keV γ line plotted against $\cos\theta$, where θ is the detection angle. The solid red line corresponds to fit according to Eq. (3).

$t = 0$) due to the scattering of the recoil nuclei as they are losing energy in the target medium. These changes in the direction should be included in the definition of $F(\tau)$. The instantaneous angle of $\beta(t)$ to the beam direction axis (z axis, say) is $\phi(t)$, such that $\beta_z(t) = \beta(t)\cos\phi(t)$, and $\beta_z(0) \equiv \beta(0)$. $F(\tau)$ is an attenuation coefficient which lies between 0 and 1. The lifetime of the γ-emitting level can be determined if $F(\tau)$ differs from 0 and 1; otherwise, a limit can be obtained for the mean lifetime. The velocity attenuation coefficient $F(\tau)$ is expressed as

$$F(\tau) = \frac{1}{v_0 \tau} \int_0^\infty \overline{v(t)\cos\phi}\, e^{-t/\tau} dt, \tag{4}$$

Here, τ is the mean lifetime of the excited states, $v(t)$ is the velocity of the recoil nuclei at time t, ϕ is the scattering angle, and $\overline{v(t)\cos\phi}$ is the time-dependent averaged projection of the recoil velocity distribution. The z component of ion velocity is changing with time as functions of the characteristic slowing-down time of the ions due to electronic processes, the initial velocity of the ions $v(0)$, the electronic and the nuclear stopping and scattering parameters. In the present

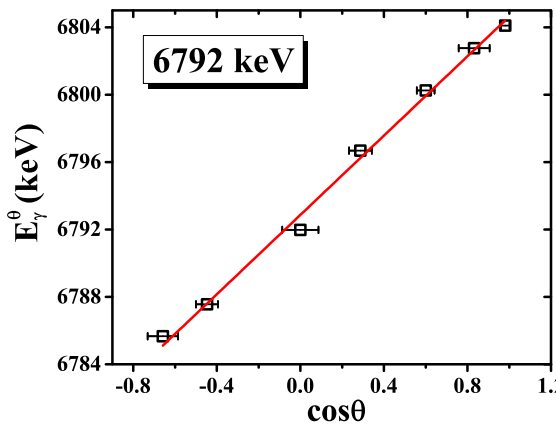

FIG. 7. Doppler shifted γ-ray energy (E_γ^θ) of 6792 keV γ line plotted against $\cos\theta$, where θ is the detection angle. The solid red line corresponds to fit according to Eq. (3).

TABLE II. Experimental $F(\tau)$ and lifetime values obtained in the present work and their comparison with previous results.

		Lifetime (τ) in fs				
E_x (keV)	$F(\tau)$	Present	Ref. [7]	Ref. [8]	Ref. [33]	Ref. [9]
5181	0.82 ± 0.03	$10.45^{+2.07}_{-2.21}$	$9.67^{+1.34}_{-1.24}$	8.40 ± 1.00	8.20 ± 1.00	–
6172	1.00 ± 0.03	<1.22	$2.10^{+1.33}_{-1.32}$	<0.77	$\leqslant$2.5	<2.5
6792	0.99 ± 0.02	<1.18	$1.60^{+0.75}_{-0.72}$	<0.77	$\leqslant$28	<1.8

work, stopping powers are taken from the SRIM 2013 [17] software. Although stoichiometry of the implanted target is not of pure Ta, the observations discussed in Ref. [21] indicate that N occupies interstitial, rather than substitutional sites within the Ta lattice as also observed by earlier workers [7,8]. Therefore, the density of the target is taken to be the same as that of pure Ta for the calculation. The value of $\overline{v(t)\cos\phi}$ has been obtained using the collision details of a large number of the ^{15}O recoiling nuclei in the Ta backing. The collision details of ^{15}O ions have been calculated using the TRIM software [17]. Then, the recoil velocity distribution was fitted with a sixth-order polynomial function. Next, Eq. (4) has been solved by replacing the $\overline{v(t)\cos\phi}$ with the fitted polynomial function. The theoretical $F(\tau)$ values for various values of τ have been calculated. As we have calculated experimental $F(\tau)$ values, for convenience of extracting corresponding τ values, $F(\tau)$ values are plotted as an independent variable in Fig. 8. The curve is fitted by a fourth-order polynomial with 95% confidence limit which expresses τ as a function of $F(\tau)$. The mean lifetime value of the 5181 keV state has been obtained from the $F(\tau)$ vs τ fitted curve with the corresponding experimental $F(\tau)$ value. In the case of 6172 keV and 6792 keV γ rays, the experimental $F(\tau)$ values are very close to 1. So, we can set upper limits of the lifetime

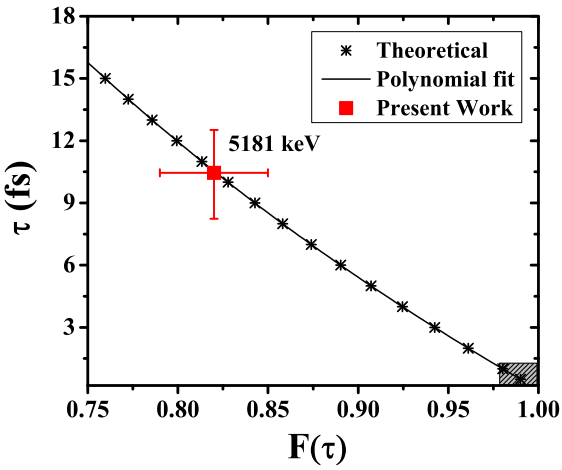

FIG. 8. The solid black line corresponds to $F(\tau)$ vs τ curve according to Eq. (4). The theoretical data points have been obtained from Eq. (4) with the help of TRIM software [17]. The grey color shaded area corresponds to the allowed region for the 6172 keV and 6792 keV γ rays for the present work. The red square corresponds to the 5181 keV γ ray. The errors associated with the $F(\tau)$ and τ values for the 5181 keV γ ray has also been shown in the figure.

values for 6172 keV and 6792 keV levels. The experimental $F(\tau)$ and lifetime values are mentioned in Table II. The errors in the lifetime values originate from the uncertainties in the stopping power taken from SRIM [17], angle measurement, target stoichiometry, etc.

IV. THEORETICAL CALCULATIONS

A. Partial wave analysis of the resonance

One of the vital parameters of resonance reaction is the width of the unbound state. In the present work, the width of the 7556 keV resonant state has been determined theoretically. The single-proton width for the capture of a proton on a quantum orbital defined by (nlj) is obtained from proton scattering cross sections calculated with a Woods-Saxon potential. The code WSPOT [34] has been utilized to calculate the phase shift and the scattering cross section as a function of (positive) energy. It searches for a resonance peak in an energy interval, and iteratively generates the full resonance curve. The resonance energy peak and the full width at half-maximum of the resonance (width of the unbound resonance state) are provided as outputs. The parameters of the potential are chosen to have the best fit of nuclear single-particle energies and nuclear radii. The program utilizes Woods-Saxon potential as the phenomenological one-body potential. The parameters of the potential are chosen to have the best fit of nuclear single-particle energies and nuclear radii [35]. The different parameters used in the present calculation are V_o(central part) $= -53$ MeV, V_1(isospin dependent part) $= -30$ MeV, and $V_{so} = 22$ MeV for the potential strengths. The radii parameters are r_o(radius parameter-central) $= r_{so}$(radius parameter-spin orbit) $= 1.25$ fm and a_o (diffuseness-central) $= a_{so}$ (diffuseness-spin orbit) $= 0.65$ fm for diffuseness. The radius for the Coulomb term is smaller with $r_c = 1.20$ fm. The variation of the energy of the incoming particle changes the relative phase of the inner and outer wave functions. The energy at which the amplitude of inside and outside wave functions match, the cross section has the maximum value. This energy is known as resonance energy. Theoretically, the one proton $1/2^+_2$ resonant state at 7556 keV is populated through a pure $l = 0$, i.e., s wave capture. By varying the energy of the incoming proton, the width of the resonance is obtained. From the theoretical calculation, we get the width of the unbound state of 1.2 keV which is close to the experimental width of 0.99(10) keV [28]. The ratio of experiment over theory provides a measure of the spectroscopic factor, $S = 0.82(9)$, which agree well with the reported experimental

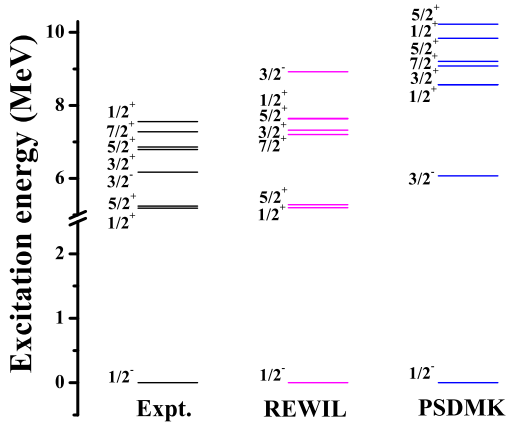

FIG. 9. Comparison of experimental energy levels with theoretical calculations of ^{15}O.

value of 0.82(18) [38]. However, it deviates by a factor of ≈0.6 from the value reported by Ref. [5].

B. Large basis shell model calculations

The rate of ^{14}N$(p,\gamma)^{15}$O resonance capture reaction depends on the structural properties of the low-lying states in ^{15}O. As discussed in Ref. [36], the proton spectroscopic factors for states in ^{15}O populated by ^{14}N$(^3$He$, d)^{15}$O reaction and neutron spectroscopic factors for ^{15}N populated by ^{14}N$(d, p)^{15}$N reaction deviate by factors of 0.65 and 0.63 for $l = 0$ and $l = 2$ components, respectively, despite being mirror partners of each other. FORTUNE [36] addressed the problem and found that the actual $l = 0$ spectroscopic factors for two $3/2^+$ states are significantly smaller than those recently reported. Thus, it is necessary to do theoretical calculations within the large basis shell model to extract the absolute spectroscopic strengths of the states of ^{15}O.

In the present work, we have used the code NUSHELLX [10] to do large basis shell model (LBSM) calculations. For a wave function and energy spectra calculation, the ZBM model space [10] has been used. The ZBM model space consists of ^{12}C core and $1p_{1/2}$, $1d_{5/2}$, and $2s_{1/2}$ as the valence orbitals. REWIL isospin interaction [37] has been used for the calculations. The energy spectra have been calculated till 20 MeV using full valence space, without any subshell restrictions. The comparison of energy levels up to 8 MeV with the experimental data is shown in Fig. 9. All the positive and negative parity states are reproduced reasonably well except the $3/2^-_1$ state, i.e., 6172 keV state which is overpredicted (see Table III). The reduced transition probabilities for $E2$ and $E1$ transitions have been calculated with effective charges $e_p = 1.35e$ and $e_n = 0.35e$, respectively. In the case of $M1$ and $M2$ transitions, standard values of intrinsic magnetic moments have been used.

The level lifetimes of the ^{15}O nucleus have been calculated by using theoretical reduced transition probabilities and experimental γ-ray energy values and branching ratios, wherever needed. The lifetime values are compared with the experimental data from the present and previous work [28]. Theory predicts the lifetime values quite well in most of the cases.

TABLE III. Comparison of experimental level energies and lifetimes of ^{15}O with the shell model predictions.

Exp.			Theory	
	Lifetime (τ)			
Energy (keV)	Present	Prev. [28]	Energy (keV)	τ
5181	$10.45^{+2.07}_{-2.21}$ fs	5.7(7) fs	5192	0.82 fs
5240	–	2.25 (21) ps	5276	1.2 ps
6172	<1.22 fs	<1.74 fs	8920	1.5 fs
6792	<1.18 fs	< 20 fs	7318	0.07 fs
6859	–	11.1(17) ps	7631	30.46 ps
7276	–	0.49(11) ps	7199	0.42 ps

Another critical parameter for astrophysical model calculations is the spectroscopic factor. The proton spectroscopic factors of the ground state, as well as the low lying states in ^{15}O, have been determined. The squares of the overlap integrals, i.e., the spectroscopic factors have been calculated for ^{14}N ground state with all the states of ^{15}O up to the resonance state. The theoretical values have been compared with the experimental data in Table IV. In most of the cases, the calculated values are closer to the experimental data report in Ref. [5]. However, for 6792 keV state, the calculated value disagrees with the experimental data. The absence of $1d_{3/2}$ orbit in the model space may be one of the reasons for this discrepancy. Interestingly the spectroscopic factor for 7556 keV from shell model agrees with the value reported in Ref. [5] which deviate by a factor of ≈0.6 from that reported by Ref. [38] as well that predicted by partial wave analysis (Sec. IV A).

It has been discussed earlier that the energy of the $3/2^-_1$ state is overpredicted and the spectroscopic factor is underpredicted. To reproduce a negative parity state $3/2^-_1$, only a single negative parity orbital $1p_{1/2}$ is present in the ZBM model space. The $1p_{3/2}$ orbital is absent in the ZBM space, which may cause the discrepancy for $3/2^-$ state.

TABLE IV. Comparison of proton spectroscopic factors of previous experimental data with the shell model predictions.

			C ^{2}S		
				Exp.	
E_x (keV)	J^π	nl_j	Theory Present	Prev. [5]	Prev. [38]
0	$1/2^-$	$1p_{1/2}$	1.23	1.29 (18)	1.7 (4)
5181	$1/2^+_1$	$2s_{1/2}$	0.01	0.004 (1)	0.0049 (15)
5240	$5/2^+_1$	$1d_{5/2}$	0.1	0.06 (1)	0.094 (20)
6172	$3/2^-_1$	$1p_{1/2}$	0.001	0.038 (16)	0.050 (11)
6792	$3/2^+_1$	$2s_{1/2}$	0.96	0.49 (1)	0.51 (11)
		$1d_{5/2}$	0.004	–	0.16 (3)
6859	$5/2^+_2$	$1d_{5/2}$	0.74	0.37 (1)	0.61 (13)
7276	$7/2^+_1$	$1d_{5/2}$	0.99	0.35 (1)	0.66 (14)
7556	$1/2^+_2$	$2s_{1/2}$	0.56	≈ 0.49	0.82 (18)

Thus, another model space PSD has been considered with PSDMK interaction. The PSD model space, consists of $1p_{3/2}$, $1d_{3/2}$ as well as $1p_{1/2}$, $1d_{5/2}$, and $2s_{1/2}$ orbitals with a ^{4}He core. In this case, full space calculations were beyond the present computational capacity. Thus a suitable truncation scheme has been adopted to perform the calculations. Subshell restrictions with six particles and two holes in the $1p_{3/2}$ orbital, zero occupancies in the $1d_{3/2}$ orbital and no restrictions to the other orbitals have been adopted. The ground state spin is reproduced, but the energy values are overpredicted (see Fig. 9). The ZBME model space ($1p_{1/2}$, $1d_{3/2}$, $1d_{5/2}$, $2s_{1/2}$) with REWILE interaction have also been used. However, the changes in the energy eigenvalues are less than 1% compared to ZBM + REWIL calculations. The inclusion of $1d_{3/2}$ orbital does not improve the results.

V. SUMMARY AND CONCLUSIONS

A few astrophysically important states of ^{15}O were populated using ^{14}N$(p,\gamma)^{15}$O resonance reaction at laboratory energy 278 keV using an implanted target. The implanted target was characterized using standard techniques and its stoichiometry was obtained using RBS data.

To get depth profile of the implanted ions in the target, it was scanned with varying proton energy from 278 keV to 312 keV. The strength of the resonance was evaluated using thick target approximation as $\Delta E \gg \Gamma$ [using Eq. (2)]. The effective stopping power was calculated using SRIM 2013 [17] software. The Ta density is used to calculate the effective stopping power. The calculated resonance strength is 12.8 (9) meV. It has been compared with previous measurements in Table I. The weighted average value of the resonance strength ($\omega\gamma_{\text{average}}$) has been found to be 12.7 (2) meV.

The lifetimes of the 6792, 6172, and 5181 keV states were measured using DSAM technique. The centroid shift method was adopted to obtain the lifetimes of the states. To calculate the velocity attenuation profile, we have used the target density of pure Ta. In the present work, we were not able to determine finite lifetime values for the 6172 and 6792 keV states. The lifetime of the subthreshold resonance state, i.e., 6792 keV was found to be $\tau < 1.18$ fs. So, the lower limit on the level width, Γ is >0.56 eV. The measurement by Galinski *et al.* [9] gave the upper limit of the lifetime for 6792 keV state as $\tau < 1.84$ fs. So, the present measurement further constrained the lifetime value of the subthreshold 6792 keV state. The obtained upper limit of the lifetime of the 6172 keV state is $\tau < 1.22$ fs. In case of 5181 keV state, we got a finite lifetime value of $10.45^{+2.07}_{-2.21}$ fs, which is in good agreement with the previous measurements [7,8].

The partial wave analysis was used to calculate the resonance width of the 7556 keV state. The calculated width of the 7556 keV state and its spectroscopic factor are in good agreement with the literature values (Ref. [38]). The theoretical calculations using LBSM with ZBM model space and REWIL interaction reproduced the experimental data well in most of the cases. The resonance state at 7556 keV is reproduced theoretically at 7646 keV using the shell model calculation. The calculated spectroscopic factor for 7556 keV state agrees with that reported in Ref. [5]. However, it disagrees with the data from Ref. [38] and the calculated value from partial wave analysis. The lifetimes and spectroscopic factors for other observed states are also calculated and compared with present and previous data, wherever available. However, some disagreements of the theoretical results with experimental data for a few states, indicate the need of improved interactions in the lighter mass region.

ACKNOWLEDGMENTS

We would like to thank all the members of ECR laboratory at TIFR, Mumbai for their help and cooperation.

[1] C. Iliadis, *Nuclear Physics of Stars* (Wiley-VCH, Weinheim, 2015).
[2] B. Chaboyer, P. Demarque, P. J. Kernan, and L. M. Krauss, Astrophys. J. **494**, 96 (1998).
[3] N. Galinski, Ph.D. thesis, University of Edinburgh, 2006.
[4] S. M. Daigle, Ph.D. thesis, University of North Carolina at Chapel Hill, 2013; S. Daigle, K. J. Kelly, A. E. Champagne, M. Q. Buckner, C. Iliadis, and C. Howard, Phys. Rev. C **94**, 025803 (2016).
[5] U. Schröder, H. W. Becker, G. Bogaert, J. Görres, C. Rolfs, H. P. Trautvetter, R. E. Azuma, C. Campbell, J. D. King, and J. Vise, Nucl. Phys. A **467**, 240 (1987).
[6] C. Angulo and P. Descouvemont, Nucl. Phys. A **690**, 755 (2001).
[7] P. F. Bertone, A. E. Champagne, D. C. Powell, C. Iliadis, S. E. Hale, and V. Y. Hansper, Phys. Rev. Lett. **87**, 152501 (2001).
[8] D. Schürmann, R. Kunz, I. Lingner, C. Rolfs, F. Schümann, F. Strieder, and H.-P. Trautvetter, Phys. Rev. C **77**, 055803 (2008).
[9] N. Galinski, S. K. L. Sjue, G. C. Ball, D. S. Cross, B. Davids, H. Al Falou, A. B. Garnsworthy, G. Hackman, U. Hager, D. A. Howell *et al.*, Phys. Rev. C **90**, 035803 (2014).
[10] B. A. Brown and W. D. M. Rae, Nucl. Data Sheets **120**, 115 (2014).
[11] S. Seuthe, H. W. Becker, A. Krauss, A. Redder, C. Rolfs, U. Schröder, H. P. Trautvetter, K. Wolke, S. Wüstenbecker, R. W. Kavanagh *et al.*, Nucl. Instrum. Methods Phys. Res. A **260**, 33 (1987).
[12] H. Y. Lee, J. Görres, H.-W. Becker, E. Stech, E. Strandberg, and M. Wiescher, Nucl. Instrum. Methods Phys. Res. B **267**, 3539 (2009).
[13] A. N. Agnihotri, A. H. Kelkar, S. Kasthurirangan, K. V. Thulasiram, C. A. Desai, W. A. Fernandez, and L. C. Tribedi, Phys. Scr. **2011**, 014038 (2011).
[14] S. Kasthurirangan, A. N. Agnihotri, C. A. Desai, and L. C. Tribedi, Rev. Sc. Instr. **83**, 073111 (2012).
[15] A. Mandal and L. C. Tribedi, Nucl. Instrum. Methods Phys. Res. B **440**, 19 (2019).

[16] A. Mandal, K. V. Thulasiram, W. Fernandes, and L. C. Tribedi, X-Ray Spectrometry **49**, 149 (2020).
[17] J. F. Ziegler and J. P. Biersack, The Stopping and Range of Ions in Matter, SRIM2013 (version 2013.00) [Online], http://srim.org.
[18] A. Bisoi, M. Saha Sarkar, C. A. Desai, L. C. Tribedi, J. Dutta, and N. R. Ray, *Production and Characterization of* ^{14}N *implanted target*, http://www.sympnp.org/proceedings [Proc. DAE Symp. Nucl. Phys. **55**, 732 (2010)].
[19] A. Bisoi, L. C. Tribedi, D. Misra, S. Biswas, K. V. Thulasiram, M. V. Rundhe, K. V. Anoop, V. Nanal, and M. Saha Sarkar, *Bulk Characterization of* ^{14}N *Implanted Target using Resonance Reaction and SIMS Measurements*, http://www.sympnp.org/proceedings [Proc. DAE Symp. Nucl. Phys. **58**, 994 (2013)].
[20] A. Bisoi, I. Ray, L. C. Tribedi, D. Misra, S. Biswas, K. V. Thulasiram, M. V. Rundhe, K. V. Anoop, V. Nanal, S. Ojha *et al.*, *Lifetime of the 6792 keV State in* ^{15}O, http://www.sympnp.org/proceedings [Proc. DAE Symp. Nucl. Phys. **60**, 892 (2015)].
[21] S. Sharma, A. Gupta, S. Das, M. Roy Chowdhury, A. Mandal, A. Bisoi, V. Nanal, L. C. Tribedi, and M. Saha Sarkar, EPJ Web Conf. **227**, 02011 (2020).
[22] M. Mayer, SIMNRA, A Simulation Program for the Analysis of NRA, RBS and ERDA, *Proceedings of the 15th International Conference on the Application of Accelerators in Research and Industry*, edited by J. L. Duggan and I. L. Morgan [Am. Inst. Phys. Conf. Proc. **475**, 541 (1999)].
[23] S. Sharma, A. Gupta, B. Dey, M. Roy Chowdhury, A. Mandal, A. Bisoi, V. Nanal, L. C. Tribedi, and M. Saha Sarkar, Nucl. Instrum. Methods Phys. Res. A **964**, 163810 (2020).
[24] S. Agostinelli, J. Allison, K. Amako, J. Apostolakis, H. Araujo, P. Arce, M. Asai, D. Axen, S. Banerjee, G. Barrand *et al.*, Nucl. Instrum. Methods Phys. Res. A **506**, 250 (2003).
[25] G. Lutter, M. Hult, G. Marissens, H. Stroh, and F. Tzika, Appl. Rad. Isotopes **134**, 200 (2018).
[26] R. Bhowmik, S. Muralithar, and R. P. Singh, *INGASORT - A New Program for the Analysis of Multi Detector Array* [Proc. DAE-BRNS Symp. Nucl. Phys. (India) **44B**, 422 (2001)], https://inis.iaea.org/search/searchsinglerecord.aspx?recordsFor=SingleRecord&RN=36070303.
[27] http://www.caen.it.
[28] http://www.nndc.bnl.gov.
[29] D. Bemmerer, F. Confortola, A. Lemut, R. Bonetti, C. Broggini, P. Corvisiero, H. Costntini, J. Cruz, A. Formicola, Z. Fülöp *et al.*, Nucl. Phys. A **779**, 297 (2006).
[30] G. Imbriani, H. Costantini, A. Formicola, A. Vomiero, C. Angulo, D. Bemmerer, R. Bonetti, C. Broggini, F. Confortola, and P. Corvisieros, Eur. Phys. J. A **25**, 455 (2005).
[31] R. C. Runkle, A. E. Champagne, C. Angulo, C. Fox, C. Iliadis, R. Longland, and J. Pollanen, Phys. Rev. Lett. **94**, 082503 (2005).
[32] H. W. Becker, W. E. Kieser, C. Rolfs, H. P. Trautvetter, and M. Wiescher, Z. Phys. A **305**, 319 (1982).
[33] F. Ajzenberg-Selove, Nucl. Phys. A **523**, 1 (1991).
[34] B. A. Brown, WSPOT code, http://www.nscl.msu.edu/~brown/reaction-codes/home.html.
[35] R. Paul, S. Sharma, S. Das, and M. Saha Sarkar, Student J. Phys. **6**, 151 (2017); https://www.iopb.res.in/~sjp/sjp_past_issues/sjp632017/5.pdf.
[36] H. T. Fortune, Phys. Rev. C **94**, 024339 (2016).
[37] J. B. McGroy and B. H. Wildenthal, Phys. Rev. C **7**, 974 (1973).
[38] P. F. Bertone, A. E. Champagne, M. Boswell, C. Iliadis, S. E. Hale, V. Y. Hansper, and D. C. Powell, Phys. Rev. C **66**, 055804 (2002).